

High-Performance Fe_xGeTe_2 -Based ($x = 4$ or 5) van der Waals Magnetic Tunnel Junctions

Baochun Wu^{1,§}, Shibo Fang^{1,§}, Jie Yang^{1,2}, Shiqi Liu^{1,3}, Yuxuan Peng¹, Qiuwei Li¹,
Zhongchong Lin¹, Junjie Shi^{1,4}, Wenyun Yang¹, Zhaochu Luo¹, Changsheng Wang¹,
Jinbo Yang^{1,4,5,6,*}, Jing Lu^{1,4,5,6,7,†} and Honglin Du^{1,3,4,‡}

¹State Key Laboratory for Mesoscopic Physics and School of Physics, Peking University, Beijing 100871, People's Republic of China

²Key Laboratory of Material Physics, School of Physics and Microelectronics, Ministry of Education, Zhengzhou University, Zhengzhou 450001, P. R. China


³Key Laboratory of Spintronics Materials, Devices and Systems of Zhejiang Province, Hangzhou 311305, China

⁴Peking University Yangtze Delta Institute of Optoelectronics, Nantong 226010, People's Republic of China

⁵Collaborative Innovation Center of Quantum Matter, Beijing 100871, People's Republic of China

⁶Beijing Key Laboratory for Magnetoelectric Materials and Devices (BKL-MEMD), Peking University, Beijing 100871, People's Republic of China

⁷Key Laboratory for the Physics and Chemistry of Nanodevice, Peking University, Beijing 100871, People's Republic of China

 (Received 13 April 2022; revised 15 November 2022; accepted 20 December 2022; published 14 February 2023)

Recently synthesized two-dimensional (2D) van der Waals (vdW) ferromagnets, Fe_xGeTe_2 ($x = 4$ and 5), have attracted great attention due to their room-temperature Curie temperature. By using *ab initio* noncollinear-spin quantum transport simulations, we predict a monotonic increasing tendency of the tunneling magnetoresistance (TMR) with increasing θ (the angle between the spins of the two electrodes) in Fe_xGeTe_2 /graphene/ Fe_xGeTe_2 vdW magnetic tunnel junctions (MTJs). The calculated maximal TMR of the two MTJs is up to 7000% and 1100% for $x = 4$ and 5 , respectively, and the former is even nearly 6 times larger than that of the commonly used MgO-based MTJ (1000% at 5 K) owing to nearly perfect spin polarization. The calculated maximal spin-transfer torque per voltage is 1–2 orders of magnitude larger than that of the MgO-based one, resulting in a reduction in the critical current for magnetization reversal by a factor of 4–5. Such high-performance 2D Fe_xGeTe_2 -based ($x = 4$ and 5) MTJs are promising for next-generation room-temperature nonvolatile memories.

DOI: [10.1103/PhysRevApplied.19.024037](https://doi.org/10.1103/PhysRevApplied.19.024037)

I. INTRODUCTION

Magnetic tunnel junctions (MTJs) are widely used in spintronics, such as magnetic random-access memory (MRAM), magnetic logic devices, and neuromorphic computing networks [1–5]. Among them, MRAM is considered as a promising substitute for currently used semiconductor RAM and is also one of the key technologies beyond complementary metal-oxide-semiconductor (CMOS) transistors [6]. Traditional bulk-based MTJs suffer from interface bonding and defects, thus generally yielding a low tunneling magnetoresistance (TMR) [7]. By contrast, the MTJs formed by stacking two-dimensional (2D) van der Waals (vdW) materials could have sharp

and flat interfaces [7], which is beneficial for overall spin-dependent tunneling, and thus, large TMR [7–14]. For example, 10⁶% TMR is observed at 1.4 K in the graphite/10-layer CrI_3 /graphite MTJ, which is much larger than the maximal TMR obtained in the traditional bulk-based MTJs (1000% theoretically and \sim 1000% at 5 K experimentally for MgO-based MTJs) [15–17]. Such an enhanced TMR will favor a higher detecting susceptibility and a higher storage density. However, one of the main obstacles that hinders these all-vdW-material-based MTJs from practical application is the fairly low Curie temperature of most 2D magnets, such as Fe_3GeTe_2 (130 K), CrI_3 (45 K), and $\text{Cr}_2\text{Ge}_2\text{Te}_6$ (30 K) [18–21]. The recently synthesized 2D ferromagnetic (FM) vdW metals Fe_xGeTe_2 ($x = 4$ and 5) are experimentally proved to have a near-room-temperature Curie temperature (270 K for 7-layer Fe_4GeTe_2 and 270–300 K for few-layer $\text{Fe}_{5-\delta}\text{GeTe}_2$), and hence, are ideal candidates for realizing practical MTJs [22–24].

*jbyang@pku.edu.cn

†jinglu@pku.edu.cn

‡duhonglin@pku.edu.cn

§B. Wu and S. Fang contributed equally to this work.

The vdW MTJs composed of metallic Fe_xGeTe_2 ($x=4$ and 5) electrodes and graphene spacer have three advantages over the extensively studied vdW MTJs composed of graphite electrodes and insulating CrI_3 spacer [7,25,26]. First, experiments show that the magnetic field needed to realize magnetization reversal in Fe_xGeTe_2 ($x=4$ and 5) (~ 0.5 T) is smaller than that in CrI_3 -based MTJs (1 T) [22,24,25]. Second, in addition to using the magnetic field, the magnetization direction of the Fe_xGeTe_2 ($x=4$ and 5) electrodes can also be reversed by an appropriate spin-polarized current utilizing the spin-transfer torque (STT) effect, but the magnetization direction of the CrI_3 spacer cannot be reversed in the same way due to its insulating nature. Third, the CrI_3 -based MTJs are volatile because the external magnetic field is needed to stabilize the FM state in CrI_3 -based MTJs [7], whereas the Fe_xGeTe_2 -based ($x=4$ and 5) MTJs are nonvolatile because the FM and antiferromagnetic (AFM) states can be stabilized without an external magnetic field or spin-polarized current, just like the $\text{Fe}_3\text{GeTe}_2/h\text{-BN}/\text{Fe}_3\text{GeTe}_2$ MTJ [7,8]. With these advantages in mind, assessing the performance of the Fe_xGeTe_2 -based ($x=4$ and 5) MTJs and revealing the internal physical mechanism will benefit the design of next-generation spintronic devices.

Here, we study the angle-dependent transport characteristics and spin-dynamic behavior of vdW $\text{Fe}_x\text{GeTe}_2/\text{graphene}/\text{Fe}_x\text{GeTe}_2$ ($x=4$ and 5) MTJs by using *ab initio* quantum transport simulations with noncollinear spin. The reliability of this method is validated by the excellent agreement between our calculated TMR [$\sim 200\%$, see details in Sec. 11 of the Supplemental Material [27]] and the experimental TMR (160%) in the $\text{Fe}_3\text{GeTe}_2/h\text{-BN}/\text{Fe}_3\text{GeTe}_2$ MTJ (see detailed methods in Sec. II) [8]. We reveal a monotonic increasing tendency of the TMR with increasing θ (the angle between the spins of the two electrodes). Remarkably, compared with the commonly used MgO-based MTJs, the maximal TMR increases by 6 times (7000%) for $x=4$, and the maximal STT per voltage is 1–2 orders of magnitude larger, resulting in a reduction in the critical current for magnetization reversal by a factor of 4–5.

II. COMPUTATIONAL METHODS

A. Geometry optimization and electronic structure calculations

The geometry optimization and electronic structure calculations of Fe_xGeTe_2 ($x=4$ and 5) are carried out using the projector-augmented-wave method with the Perdew-Burke-Ernzerhof (PBE) generalized gradient approximation (GGA) [28], as implemented in the VASP package [29–31]. The Monkhorst-Pack k -point mesh is sampled with a separation of about 0.01 \AA^{-1} in the 2D Brillouin zone. The ionic relaxation for structure optimization stops when the residual force on each atom is less than 0.01 eV \AA^{-1} . The

energy cutoff is 440 eV for the plane-wave basis expansion with the total-energy convergence criteria of $1 \times 10^{-4} \text{ eV}$ per unit cell. The vdW-D2 approach is adopted to describe the interlayer vdW interaction. The Hubbard U value is set as zero for two reasons. First and foremost, both previous calculations and our calculation results show that the GGA + PBE calculation results with $U=4.3 \text{ eV}$ overestimate the average magnetic moment, m , of the Fe atoms in Fe_5GeTe_2 ($> 2.4 \mu_B$), compared with experimental data ($1.80 \mu_B$) [22,32]. The obtained m ($1.7 \mu_B$) without Hubbard U is much closer to the experiment results. Second, previous calculations also show that the geometry for bulk Fe_5GeTe_2 obtained from the GGA + PBE function without Hubbard U is closer to experimental data. In contrast, the calculation results with $U=4.3 \text{ eV}$ overestimate the lattice parameter a .

B. Transport-property calculations with noncollinear spin

For the MTJs, the spin-resolved transport characteristics are simulated by using density-functional theory (DFT) coupled with the nonequilibrium Green function (NEGF) formalism, as implemented in the QuantumATK 2020 software package [33,34]. The exchange-correlation interaction here is represented by the noncollinear generalized gradient approximation (NCGGA) in the form of the PBE potential. The double-zeta-polarized (DZP) set is used. The real-space density mesh cutoff is taken as 100 Hartree. The k -point meshes for the electrode region and the central region are $7 \times 7 \times 21$ and $7 \times 7 \times 1$, respectively. The boundary conditions are period-, period-, and Dirichlet-type conditions along the x , y , and z directions (z is the transport direction), respectively. We use 300 K as the temperature for the Fermi-Dirac distribution of electrons in our transport calculations, and we do not include the scattering of the phonons.

In our calculations, the noncollinear transmission coefficient, $t_{\alpha\beta}^{k_{\parallel}}(E)$ (k_{\parallel} stands for the reciprocal lattice vector along the surface-parallel direction in the irreducible Brillouin zone; α and β stand for \uparrow or \downarrow), is represented by [35–37]

$$t_{\alpha\beta}^{k_{\parallel}}(E) = \text{Tr}[n_{\alpha\beta}\Gamma_l^{k_{\parallel}}(E)G^{k_{\parallel}}(E)\Gamma_r^{k_{\parallel}}(E)G^{k_{\parallel}\dagger}(E)], \quad (1)$$

where $n_{\alpha\beta}$ is any component of the density matrix in the spin Hilbert space; $G^{k_{\parallel}}(E)$ and $G^{k_{\parallel}\dagger}(E)$ stand for the retard and advanced Green's function, respectively.

$G^{k_{\parallel}}(E) = \left[(E + i\delta_+)I^{k_{\parallel}} - H^{k_{\parallel}} - \sum_l^{k_{\parallel}}(E) - \sum_r^{k_{\parallel}}(E) \right]^{-1}$, where δ_+ is an infinitesimally positive number, $I^{k_{\parallel}}$ is the identity matrix, $H^{k_{\parallel}}$ is the Hamiltonian matrix, and $\sum_{l(r)}^{k_{\parallel}}(E)$ is the self-energy matrix. $\Gamma_{l(r)}^{k_{\parallel}}(E) = i \left(\sum_{l(r)}^{k_{\parallel}} - \sum_{l(r)}^{k_{\parallel}\dagger} \right)$ is the broadening function originating

from the left (right) electrode in the form of self-energy $\sum_{l(r)}^{k_{\parallel}}$. Given a certain energy, the transmission function $t_{\alpha\beta}(E)$ is obtained by averaging the transmission coefficient, $t_{\alpha\beta}^{k_{\parallel}}(E)$, over all different k_{\parallel} in the irreducible Brillouin zone. The k -point meshes used for calculating conductance are 150×150 . As shown in Fig. S4 within the Supplemental Material [27], we take $G_{\text{sum}}(0^\circ)$ and $G_{\text{sum}}(180^\circ)$ in the $\text{Fe}_4\text{GeTe}_2/\text{graphene}/\text{Fe}_4\text{GeTe}_2$ MTJ as an example to clarify the k -point convergence for conductance and TMR. n_k refers to the $n_k \times n_k$ k -point meshes. As n_k increases, the variation tendency of $G_{\text{sum}}(0^\circ)$ and $G_{\text{sum}}(180^\circ)$ gradually flattens out. When n_k increases from 140 to 150, $G_{\text{sum}}(0^\circ)$ and $G_{\text{sum}}(180^\circ)$ approximately remain unchanged. So, we adopt the 150×150 k -point meshes to calculate the transport properties in the Fe_xGeTe_2 -based ($x = 4$ and 5) MTJs.

C. Gilbert-damping-factor calculations

The critical current for magnetization switching is related to the Gilbert damping factor. The unitless Gilbert damping tensor is calculated using Kambersky's torque-torque correlation model, which can be written as [38,39]

$$\alpha_{\mu,\nu} = \frac{g}{m\pi} \sum_k \omega_k \sum_{ij} W_{ij}(k) T_{ij}^{\nu}(k) (T_{ij}^{\mu}(k))^{\dagger}, \quad (2)$$

where $g = 2.0023$ is the g factor; m is the magnetization (has units of Bohr magnetons). The sum over ij runs over the band indices, and the k sum is over the Brillouin zone with ω_k being the k -point weight. The matrix elements of the torque operator are

$$T_{ij}^{\nu}(k) = \langle \varphi_{ik} | [\sigma^{\nu}, H_{\text{SO}}] | \varphi_{jk} \rangle, \quad (3)$$

where σ^{ν} is a Pauli spin matrix, H_{SO} is the spin-orbit contribution to the Hamiltonian, and φ_{ik} is the Bloch eigenstate of band n evaluated at k -point k . The spectral overlap function is

$$W_{ij}(k) = \int \left(-\frac{\partial f(\varepsilon, \varepsilon_F)}{\partial \varepsilon} \right) A_{ik}(\varepsilon, \Lambda) A_{jk}(\varepsilon, \Lambda) d\varepsilon, \quad (4)$$

where $f(\varepsilon, \varepsilon_F)$ is the Fermi-Dirac distribution function (ε_F is the Fermi energy), and $A_{ik}(\varepsilon, \Lambda) = 1/\pi(\Lambda/(\Lambda^2 + (\varepsilon_{ik} - \varepsilon)^2))$ is a Lorentzian spectral function with broadening Λ and centered around the band energy ε_{ik} . Assuming that the spectral lifetime broadening, Λ , mainly originates from electron-phonon coupling, it is reasonable to assume that $\Lambda > k_B T$; in which case, we can approximate the derivative of the Fermi-Dirac distribution by a δ function resulting in the simplified expression

$$W_{ij}(k) \approx A_{ik}(\varepsilon_F, \Lambda) A_{jk}(\varepsilon_F, \Lambda), \quad (5)$$

as implemented in the QuantumATK 2020 software package [38,39]. The Monkhorst-Pack k -point mesh used here

for bilayer (BL) Fe_xGeTe_2 ($x = 4$ and 5) is $35 \times 35 \times 1$. The diagonal terms of the Gilbert damping tensor play the major role. Thus, the Gilbert damping factor, α , in this work is obtained as $\alpha = \alpha_{xx} + \alpha_{yy} + \alpha_{zz}$.

D. Magnetocrystalline anisotropic energy calculations

The magnetocrystalline anisotropic energy, E_{MCA} , is calculated by the "force theorem." Upon inclusion of spin-orbit coupling (SOC), the force theorem expresses E_{MCA} as the difference of band energies between two spin orientations for a particular projection " p " (an atom or orbital projection) as [40]

$$E_{\text{MCA}} = \left| \sum_{n,k} f_{n,k}(\theta, \varphi) \varepsilon_{n,k}(\theta, \varphi) \omega_{n,k}^p(\theta, \varphi) - \sum_{n,k} f_{n,k}(0^\circ, 0^\circ) \varepsilon_{n,k}(0^\circ, 0^\circ) \omega_{n,k}^p(0^\circ, 0^\circ) \right|, \quad (6)$$

where $f_{n,k}$ is the occupation factor for band index n and wave vector k ; the spherical angle (θ, φ) describes the spin orientation [we set the initial spin orientation as $(0^\circ, 0^\circ)$]; $\varepsilon_{n,k}(\theta, \varphi)$ is the corresponding band energy; and $\omega_{n,k}^p$ is the projection weight, which is

$$\omega_{n,k}^p = \left\langle \varphi_{n,k} \left| \frac{\mathbf{S}\mathbf{P} + \mathbf{P}\mathbf{S}}{2} \right| \varphi_{n,k} \right\rangle \quad (7)$$

with $\varphi_{n,k}$ as the eigenstate; \mathbf{S} is the overlap matrix and \mathbf{P} is the projection matrix. \mathbf{P} is a diagonal singular matrix, with the indices corresponding to the orbitals we wish to project onto. $E_{\text{MCA}}^i = \sum_p E_{\text{MCA}}^i|_p$ with p going over all the orbitals of the i th atom. It is the absolute energy difference that we substitute into our estimate of the critical current, so we add the sign of the absolute value. The Monkhorst-Pack k -point mesh used here for BL Fe_xGeTe_2 ($x = 4$ and 5) is $36 \times 36 \times 1$.

E. STT calculations

STT is calculated using the linear-response method, as implemented in the QuantumATK 2020 software package [40–42]. Under this framework, only a small bias voltage, δV_b , is applied across the junction. The STT, here denoted \mathbf{Q} , is expressed as

$$\mathbf{Q} = \text{Tr}(\delta \rho_{\text{NEQ}} \sigma \times \mathbf{B}_{\text{XC}}). \quad (8)$$

Based on this relationship, we can evaluate the linear-response coefficient of the torque with the bias voltage, i.e., the so-called spin-transfer torque (STTK) on an atom

site a , τ^a , as

$$\tau^a = \frac{\delta Q^a}{\delta V_b}. \quad (9)$$

The linear-response STT (\mathbf{T}) can be obtained by integrating τ^a over the corresponding regions of the device, that is,

$$\mathbf{T} = \sum_a \tau^a, \quad (10)$$

where a takes all the atoms in the corresponding region.

The Monkhorst-Pack k -points mesh used for the STT calculation in our $\text{Fe}_x\text{GeTe}_2/\text{graphene}/\text{Fe}_x\text{GeTe}_2$ ($x=4$ and 5) MTJs is $180 \times 180 \times 1$.

F. Reliability of the DFT + NEGF method

The reliability of the DFT + NEGF method in predicting MR and STT is validated by the agreement between the theoretically predicted values and the experimental values. For the $\text{Fe}_3\text{GeTe}_2/h\text{-BN}/\text{Fe}_3\text{GeTe}_2$ MTJ, previous calculations based on the combination of DFT and the wave-function-scattering method overestimate the TMR by an order of magnitude (6256%) [43]. By contrast, the calculated TMR value of about 200% (this work, see Sec. 11 of the Supplemental Material [27]) by using the DFT + NEGF method is in agreement with the experimental value of 160% [8]. The calculated TMR obtained by using the DFT + NEGF method is also consistent with the experimental results in the graphite/ n -layer- CrI_3 /graphite MTJ [14,25,26]. The measured in-plane STTK reported by Sankey *et al.* for the

$\text{Fe}/\text{MgO}/\text{Fe}$ MTJ [$3.5 \times 10^{10} (\Omega\text{m}^2)^{-1}$] agrees quantitatively with the calculated value using the DFT + NEGF method [44,45].

III. RESULTS AND DISCUSSION

A. Electronic structures of Fe_xGeTe_2 ($x=4$ and 5)

We start by clarifying the electronic structures of BL Fe_xGeTe_2 ($x=4$ and 5). The optimized structures of BL Fe_4GeTe_2 (Fe_5GeTe_2) are shown in Figs. 1(a) and 1(b) [1(d) and 1(e)] (for details about the geometric structures, see Sec. 1 of the Supplemental Material [27]) [46]. The spin-resolved band structures and density of states (DOS) of BL Fe_4GeTe_2 (Fe_5GeTe_2) at the FM ground state are shown in Figs. 1(c) [1(f)]. BL Fe_xGeTe_2 ($x=4$ and 5) are both typical magnetic metals, and our calculated band structures are very similar to the previous calculation results of the corresponding bulk [32,46], indicating weak interlayer coupling. Figure S2 presents the corresponding calculation results with SOC correction (see Sec. 2 of the Supplemental Material [27]). The comparison shows that the SOC has little effect on the electronic structures of BL Fe_xGeTe_2 ($x=4$ and 5). For the sake of simplicity and convenience, we define $D_\sigma(E_f)$ ($\sigma = \uparrow$ or \downarrow) as the spin-resolved DOS of the σ -spin electrons at the Fermi level, E_f , and P^D as the polarizability of DOS at E_f , that is,

$$P^D = \frac{D_\uparrow(E_f) - D_\downarrow(E_f)}{D_\uparrow(E_f) + D_\downarrow(E_f)} \times 100\%. \quad (11)$$

From Figs. 1(c) [1(f)], for BL Fe_4GeTe_2 (Fe_5GeTe_2), $D_\uparrow(E_f) = 6.0(7.5)$ states/eV, $D_\downarrow(E_f) = 1.7(5.1)$ states/eV,

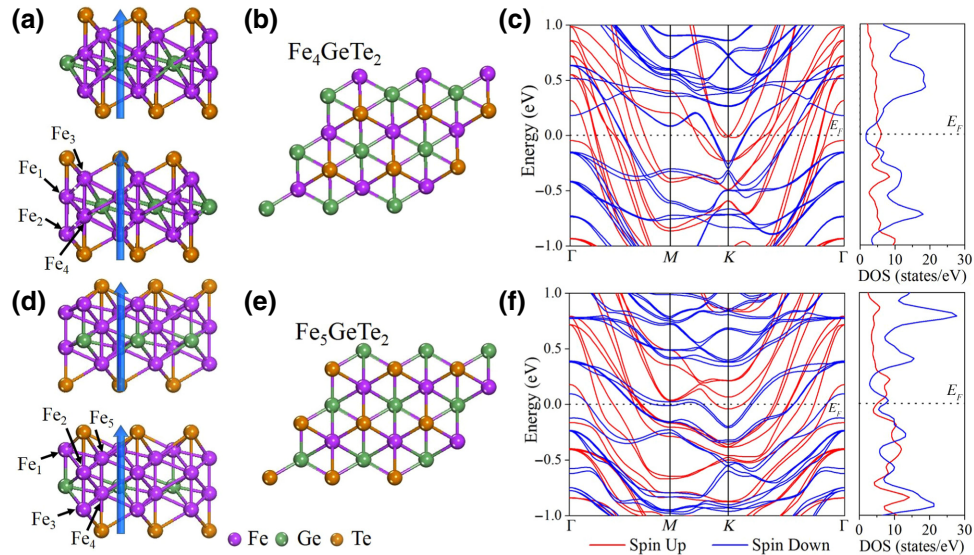


FIG. 1. Side (a) [(d)] and top (b) [(e)] views of the atomic structure of BL Fe_4GeTe_2 (Fe_5GeTe_2). Blue arrows represent the magnetic moment of all the Fe atoms in each layer. Spin-resolved band structures and DOS of BL Fe_4GeTe_2 (c) and BL Fe_5GeTe_2 (f). Fermi level is set to zero.

and $P^D = 55.8\%$ (19%). The different P^D is one of the main reasons for the different transport properties between the two similar structures, as shown next.

B. Transport properties of $\text{Fe}_x\text{GeTe}_2/\text{graphene}/\text{Fe}_x\text{GeTe}_2$ ($x = 4$ and 5) MTJs with noncollinear spin

We use AB -stacking BL Fe_xGeTe_2 ($x = 4$ and 5) as the electrodes and monolayer (ML) graphene as the spacer to build the MTJs (see Sec. 3 of the Supplemental Material for the reason why we use the bilayer structure for

the electrodes, and the effect of the stacking order on our calculation results [27]), as shown in Figs. 2(a) and 2(b). When building the device model, we use the $\sqrt{3} \times \sqrt{3}$ in-plane unit cell of graphene to match the unit cell of Fe_xGeTe_2 ($x = 4$ and 5) at the interface (see Sec. 10 of the Supplemental Material for the selection of the interface, the influence of the relative shift at the interface, and the reason why we mainly use graphene as the spacer [27]). Rotation between the two surfaces is 150° . The mean absolute strain to both surfaces, which is mainly in the in-plane direction, is less than 2%. The whole device structure is optimized using VASP with the vdW-D2 correction (see

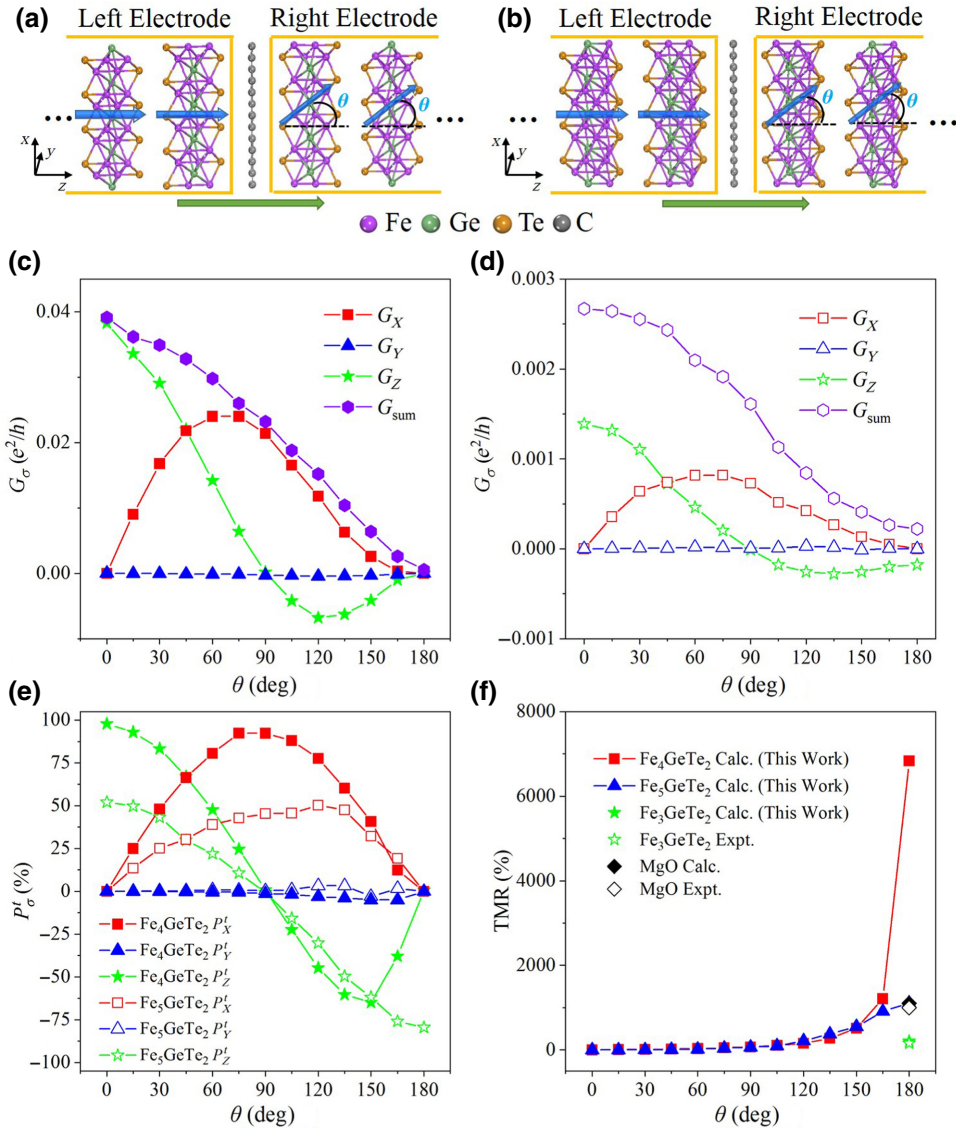


FIG. 2. Device model for $\text{Fe}_4\text{GeTe}_2/\text{graphene}/\text{Fe}_4\text{GeTe}_2$ (a) and $\text{Fe}_5\text{GeTe}_2/\text{graphene}/\text{Fe}_5\text{GeTe}_2$ (b) MTJs. Yellow lines surround the electrode region. Blue arrows indicate the magnetic moment of all the Fe atoms in each layer. Green arrows indicate the transport direction. θ represents the angle between the magnetization directions of the two electrodes. θ -dependent noncollinear-spin projections of conductance at $E = E_F$ for $\text{Fe}_4\text{GeTe}_2/\text{graphene}/\text{Fe}_4\text{GeTe}_2$ (c) and $\text{Fe}_5\text{GeTe}_2/\text{graphene}/\text{Fe}_5\text{GeTe}_2$ (d) MTJs. θ -dependent noncollinear-spin polarizability (e) and TMR (f). Theoretically and experimentally reported TMR values (they are close to each other) of the Fe_3GeTe_2 -based MTJ and MgO-based MTJ are also provided for comparison.

Sec. II for details). The deformation of the overall structure is indeed very small, indicating that the mismatch between the $\sqrt{3} \times \sqrt{3}$ in-plane unit cell of graphene and the unit cell of Fe_xGeTe_2 ($x=4$ and 5) is very small. The maximum difference between the z coordinates of all C atoms is about 0.004 \AA , indicating that there is nearly no structural change in graphene. The optimized distance between the ML graphene and the adjacent Fe_4GeTe_2 (Fe_5GeTe_2) layer is 3.49 \AA (3.50 \AA), indicating the weak vdW interaction across the interface. For comparison, the Fe-MgO interface distance in the Fe/MgO/Fe MTJ is about 2.16 \AA [17]. We set the initial magnetization direction of both electrodes along the z axis. Then we fix the magnetization direction of the left electrode and rotate the magnetization direction of the right electrode by angle θ (0° – 180°) towards the x axis (still in the x - z plane). During this process, we evaluate the effect of θ on the transport properties of these MTJs. Note that, when $\theta = 0^\circ$ (180°), it is equivalent to the collinear FM (AFM) case.

Under the framework of noncollinear spin, the spin can no longer be simply decomposed into \uparrow and \downarrow . Instead, the eigenstate in the spin Hilbert space becomes a spinor with a certain mixing of both spin-up and -down channels. Therefore, the density matrix in the spin Hilbert space can be defined as [47]

$$\mathbf{n} = \begin{bmatrix} n_{\uparrow\uparrow} & n_{\uparrow\downarrow} \\ n_{\downarrow\uparrow} & n_{\downarrow\downarrow} \end{bmatrix}. \quad (12)$$

Note that, when it goes back to the collinear case ($\theta = 0^\circ$ or 180°), the $\uparrow\downarrow$ and $\downarrow\uparrow$ components are both equal to zero, and the $\uparrow\uparrow$ ($\downarrow\downarrow$) component corresponds to the spin-up (-down) component. Correspondingly, the calculated θ -dependent noncollinear transmission function at $E = E_f$ of the MTJs can be expressed as

$$\mathbf{t}(\theta) = \begin{bmatrix} t_{\uparrow\uparrow}(\theta) & t_{\uparrow\downarrow}(\theta) \\ t_{\downarrow\uparrow}(\theta) & t_{\downarrow\downarrow}(\theta) \end{bmatrix}. \quad (13)$$

We can derive a range of different spin projections from the four basic components of $\mathbf{t}(\theta)$, utilizing a projection rule relevant to the Pauli matrix, that is,

$$t_{\text{sum}}(\theta) = t_{\uparrow\uparrow}(\theta) + t_{\downarrow\downarrow}(\theta), \quad (14)$$

$$t_X(\theta) = 2 \text{Re}(t_{\uparrow\downarrow}(\theta)), \quad (15)$$

$$t_Y(\theta) = 2 \text{Im}(t_{\uparrow\downarrow}(\theta)), \quad (16)$$

$$t_Z(\theta) = t_{\uparrow\uparrow}(\theta) - t_{\downarrow\downarrow}(\theta), \quad (17)$$

where the subscripts ‘‘sum,’’ ‘‘X,’’ ‘‘Y,’’ and ‘‘Z’’ stand for spin sum, spin X , spin Y , and spin Z , respectively.

Then we can define θ - and noncollinear-spin-dependent conductance of the MTJs, $G_\sigma(\theta)$, at $E = E_f$ as

$$G_\sigma(\theta) = \frac{e^2}{h} t_\sigma(\theta), \sigma = \text{sum}, X, Y, \text{ and } Z. \quad (18)$$

Note that, when $\theta = 0^\circ$ and 180° , $t_{\uparrow\downarrow}$ and $t_{\downarrow\uparrow}$ are both approximately equal to 0, and the definition of G_{sum} is consistent with the definition of the total conductance in the collinear-spin situation. Another point is that, from a physical point of view, G_σ ($\sigma = X, Y$, and Z) corresponds only to the conductance part with pure spin current. Additionally, G_σ ($\sigma = X, Y$, and Z) does not include the conductance part with zero spin current. The total conductance, G_{sum} , includes the conductance of all the electrons. To make it clearer, we can take the spin- Z electrons as an example, since the definitions are based on the fact that the z direction is the transport direction. Similar to the spin-up and spin-down electrons in the collinear-spin situation, the spin- Z electrons in the noncollinear-spin situation can also be divided into spin- $+Z$ electrons (corresponding to $t_{\uparrow\uparrow}$) and spin- $-Z$ electrons (corresponding to $t_{\downarrow\downarrow}$). The conductance part with zero spin current corresponds to the conductance of the group of electrons with the same number of spin- $+Z$ and spin- $-Z$ electrons. G_Z (defined as $(e^2/h)(t_{\uparrow\uparrow} - t_{\downarrow\downarrow})$) represents the conductance of the electrical spin current, that is, the conductance of spin- $+Z$ electrons minus the conductance of spin- $-Z$ electrons. G_{sum} [defined as $(e^2/h)(t_{\uparrow\uparrow} + t_{\downarrow\downarrow})$] includes the conductance of all the electrons, irrespective of the spin-polarized direction. We can assume a simple situation where $t_{\uparrow\uparrow} = 3$, $t_{\downarrow\downarrow} = 1$, and $t_{\uparrow\downarrow} = t_{\downarrow\uparrow} = 0$. Here, we omit the common unit (e^2/h) , then we can get $G_X = G_Y = 0$, $G_Z = 3 - 1 = 2$, and $G_{\text{sum}} = 3 + 1 = 4$. The conductance part with zero spin current is $1 + 1 = 2$, and the spin polarizability is $(3 - 1/3 + 1) = 50\%$. It is also obvious that $G_{\text{sum}} \neq G_X + G_Y + G_Z$.

Figures 2(c) and 2(d) show the calculated $G_\sigma(\theta)$ of the two MTJs, and the variation tendency with θ is very similar between the two MTJs. G_Y fluctuates around zero because the magnetization directions of both electrodes remain in the x - z plane, and thus, the scattering for spin- Y electrons is always strong. G_{sum} generally decreases with increasing θ , which is due to the mismatch between the electronic structures of the left electrode and right electrode during the rotation process. As angle θ increases, the mismatch also increases, which is manifested by the calculated k_{\parallel} -resolved transmission coefficients of the MTJs shown in Figs. 3 and 4. The contributing transmission channels (with nonvanishing k_{\parallel} -resolved transmission coefficients $t^{k_{\parallel}}$) directly determine the magnitude of G . So, we can directly see that the overall tunneling of the $\text{Fe}_4\text{GeTe}_2/\text{graphene}/\text{Fe}_4\text{GeTe}_2$ MTJ is stronger than that of the $\text{Fe}_5\text{GeTe}_2/\text{graphene}/\text{Fe}_5\text{GeTe}_2$ MTJ. Meanwhile,

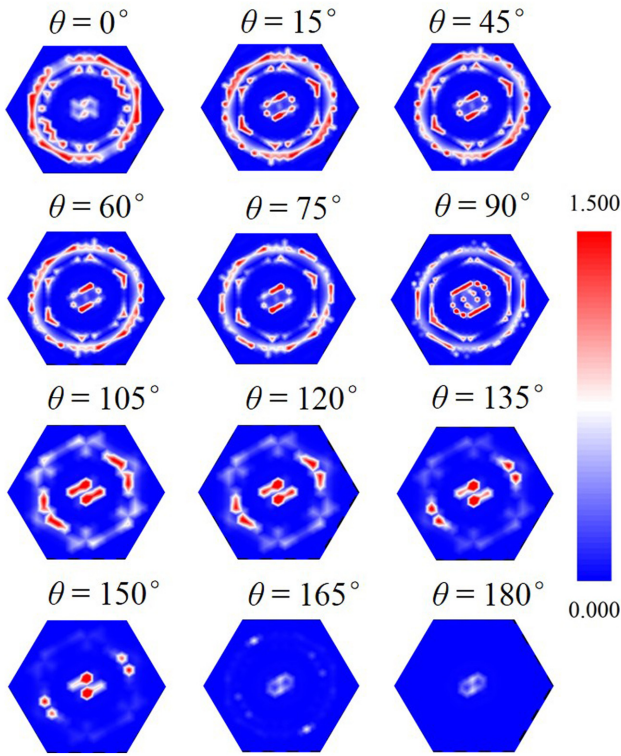


FIG. 3. θ -dependent k_{\parallel} -resolved transmission coefficients across the $\text{Fe}_4\text{GeTe}_2/\text{graphene}/\text{Fe}_4\text{GeTe}_2$ MTJ in the Brillouin zone calculated at E_F . Linear scale bar is adopted.

the number of contributing transmission channels generally decreases with increasing θ . Another feature shown in Figs. 3 and 4 is that the transmission patterns show twofold symmetry in the 2D Brillouin zone (BZ) for all the angles. The symmetry of the k_{\parallel} -resolved transmission coefficients is mainly determined by the 180° rotational symmetry of the electrodes. Figure S12 within the Supplemental Material [27] shows the top view and side view of the unit cell of BL Fe_xGeTe_2 ($x=4$ and 5). If we rotate the AB -stacking BL Fe_4GeTe_2 180° around the z axis that passes the center of the unit cell, it turns into BA -stacking BL Fe_4GeTe_2 , and this does not affect the transmission patterns at zero bias. For AB -stacking BL Fe_5GeTe_2 , the situation is exactly the same. The distribution of the k_{\parallel} -resolved transmission coefficients in the 2D BZ largely depends on the Fermi surfaces of the electrodes and the spacer (k_{\parallel} is conserved during the transmission process). Figure 5 shows the total Fermi surfaces of BL Fe_xGeTe_2 ($x=4$ and 5) electrodes projected in the 2D BZ perpendicular to the transport direction. The patterns both possess twofold symmetry, which is consistent with the symmetry of the geometric structures. The distribution of the transmission channels shown in Figs. 3 and 4 resembles the distribution of the Fermi surfaces of the BL Fe_xGeTe_2 ($x=4$ and 5) electrodes, which is more obvious for the $\text{Fe}_4\text{GeTe}_2/\text{graphene}/\text{Fe}_4\text{GeTe}_2$ MTJ. Coupling

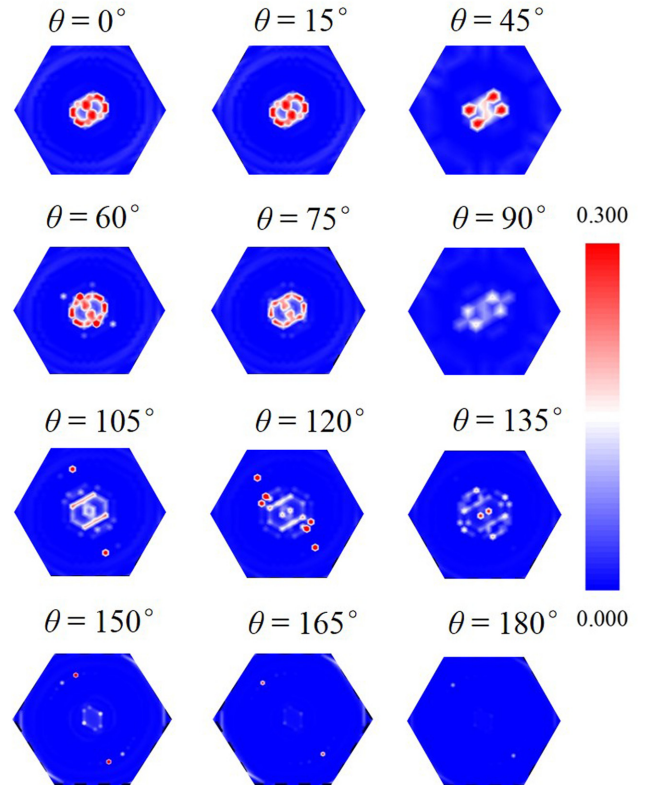


FIG. 4. θ -dependent k_{\parallel} -resolved transmission coefficients across the $\text{Fe}_5\text{GeTe}_2/\text{graphene}/\text{Fe}_5\text{GeTe}_2$ MTJ in the Brillouin zone calculated at E_F . Linear scale bar is adopted.

with the graphene spacer filters out some originally available transmission channels, especially at the edge of the 2D BZ. For the $\text{Fe}_5\text{GeTe}_2/\text{graphene}/\text{Fe}_5\text{GeTe}_2$ MTJ, the magnitude of overall tunneling is smaller, and the transmission channels tend to be distributed near the Γ point.

To better clarify the reasons for the variation tendency of the transport properties, we can define two kinds of matching rates that measure the degree of matching in transport in the MTJ. One measures how well the electrode matches the spacer (defined as η_s), which is mainly determined by

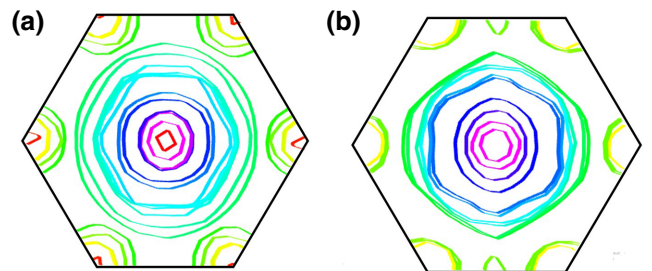


FIG. 5. Spin-sum Fermi surfaces of the BL Fe_4GeTe_2 (a) and Fe_5GeTe_2 (b) electrodes projected in the 2D BZ perpendicular to the transport direction. Different colors represent contributions from different bands.

the materials of the electrode and the spacer and the interfacial quality. The other measures how well the left electrode matches the right electrode (defined as η_e), which is mainly determined by the materials and electronic structures of the two electrodes. Rotating the magnetization direction of the right electrode changes its electronic structures. Therefore, as θ increases, η_e decreases, leading to decreasing G_{sum} . Despite the similar relative variation tendency with θ , the difference in the absolute value of G_{sum} between the two MTJs can be attributed to two aspects: one is the intrinsic properties of the electrodes, mainly corresponding to the different $D_\sigma(E_f)$ of BL Fe₄GeTe₂ and Fe₅GeTe₂; the other is the properties of the junction, mainly corresponding to different η_s and η_e in the two MTJs.

As shown in Figs. 2(c) and 2(d), G_X first increases with increasing θ before it starts to decrease with increasing θ . The nonmonotonic behavior of G_X is the result of competition between two factors. One is the decreasing tendency due to decreasing η_e stated above. The other is the change of the right electrode's spin-filtering effect with increasing θ . When θ increases from 0° to 90° , the right electrode's spin-filtering effect on spin- X electrons becomes weaker, resulting in the increase of G_X . When θ increases from 90° to 180° , the situation is exactly the opposite for G_X . G_Z keeps decreasing with increasing θ until G_Z reaches zero, and then G_Z increases in the opposite direction before it finally decreases with increasing θ . We can understand the effect of the two factors (η_e and the right electrode's spin-filtering effect) from the definition of G_Z [defined as $(e^2/h)(t_{\uparrow\uparrow} - t_{\downarrow\downarrow})$]. As θ increases, η_e decreases, leading to a decreasing tendency for both $t_{\uparrow\uparrow}$ and $t_{\downarrow\downarrow}$. As θ increases from 0° to 180° , the right electrode's spin-filtering effect on spin- $+Z$ electrons monotonically increases. Therefore, we get a monotonically decreasing $t_{\uparrow\uparrow}$. As θ increases from 0° to 180° , the right electrode's spin-filtering effect on spin- $-Z$ electrons monotonically decreases, leading to the increasing tendency for $t_{\downarrow\downarrow}$. The combination of the two factors causes $t_{\downarrow\downarrow}$ to first increase and then decrease with increasing θ , and the turning point is generally around $\theta = 90^\circ$. Therefore, the nonmonotonic behavior of G_Z originates from the nonmonotonic behavior of $t_{\downarrow\downarrow}$. The negative value of G_Z when $\theta > 90^\circ$ indicates that the direction of the spin current is $-Z$.

The θ -dependent noncollinear-spin polarization of the two MTJs, $P'_\sigma(\theta)$, at $E = E_F$ is shown in Fig. 2(e) and defined as

$$P'_\sigma(\theta) = \frac{G_\sigma(\theta)}{G_{\text{sum}}(\theta)}, \sigma = X, Y, \text{ and } Z. \quad (19)$$

Note that, when $\theta = 0^\circ$ and 180° , the definition of P'_Z is consistent with the definition of spin polarization in the collinear-spin situation. $P'_\sigma(\theta)$ reflects the contribution of the conductance part with pure spin current to the total conductance. For practical electrode materials in the MTJs,

$P'_Z(0^\circ)$ is generally less than 100%. For similar MTJ configurations, $P'_Z(0^\circ)$ generally increases as the spin-filtering efficiency of the electrode material increases.

The variation tendency of $P'_\sigma(\theta)$ is generally derived from the variation tendency of $G_\sigma(\theta)$ for both MTJs. As G_Y fluctuates around zero, P'_Y also fluctuates around zero. As G_X first increases and then decreases with increasing θ , P'_X also first increases and then decreases with increasing θ . The location of the turning point depends on the relative decline rates of G_X and G_{sum} . The variation tendency of P'_Z is also the combination of the decreasing tendency of G_{sum} and the variation tendency of G_Z . Nearly 100% $P'_Z(0^\circ)$ is observed in the Fe₄GeTe₂/graphene/Fe₄GeTe₂ MTJ, indicating perfect spin-filtering efficiency (SFE), whereas only 54% $P'_Z(0^\circ)$ is obtained in the Fe₅GeTe₂/graphene/Fe₅GeTe₂ MTJ, indicating a much weaker SFE.

Figure S5 within the Supplemental Material [27] shows the spin-resolved transmission eigenstates at E_F in the Fe_xGeTe₂/graphene/Fe_xGeTe₂ ($x = 4$ and 5) MTJ, which visualizes the overall transport and spin-filtering effect in the two MTJs when θ is equal to 0° (FM) and 180° (AFM). For both MTJs in the FM state, most of the spin-up ($\uparrow\uparrow$) electrons can tunnel through the barrier and reach the other electrode, whereas the spin-down ($\downarrow\downarrow$) electrons are mostly blocked in the channel. For both MTJs in the AFM state, both the spin-up ($\uparrow\uparrow$) and spin-down ($\downarrow\downarrow$) electrons are mostly blocked in the channel. If we make a comparison between the transmission eigenstates of these two MTJs in the FM state, we can find that the total number of electrons (reflected by the number of isosurfaces) that can tunnel through the barrier in the Fe₄GeTe₂/graphene/Fe₄GeTe₂ MTJ is obviously larger than that in the Fe₅GeTe₂/graphene/Fe₅GeTe₂ MTJ, and the difference between the numbers of spin-up ($\uparrow\uparrow$) and spin-down ($\downarrow\downarrow$) electrons that can tunnel through the barrier in the Fe₄GeTe₂/graphene/Fe₄GeTe₂ MTJ is also larger than that in the Fe₅GeTe₂/graphene/Fe₅GeTe₂ MTJ. The former corresponds to the relative size of G_{sum} , and the latter corresponds to the relative size of $P'_Z(0^\circ)$. The higher $P'_Z(0^\circ)$ of the Fe₄GeTe₂/graphene/Fe₄GeTe₂ MTJ over the Fe₅GeTe₂/graphene/Fe₅GeTe₂ MTJ can be attributed to the higher P^D of the electrodes and the different η_s of the two MTJs. Generally speaking, $P'_Z(0^\circ)$ is positively correlated with P^D (or η_s).

Figure 6 shows the calculated weight-projected band structures of the Fe_xGeTe₂/graphene/Fe_xGeTe₂ ($x = 4$ and 5) MTJs. Similar to the previously reported Fe₃GeTe₂/graphene/Fe₃GeTe₂ MTJ [43], the K and K' points for the $\sqrt{3} \times \sqrt{3}$ unit cell of graphene are located at the Γ point in the MTJs. Although the band structures of graphene and Fe_xGeTe₂ ($x = 4$ and 5) retain most of their characteristics, which indicates that the vdW interaction plays the leading role, their hybridization and offset are still more obvious than those

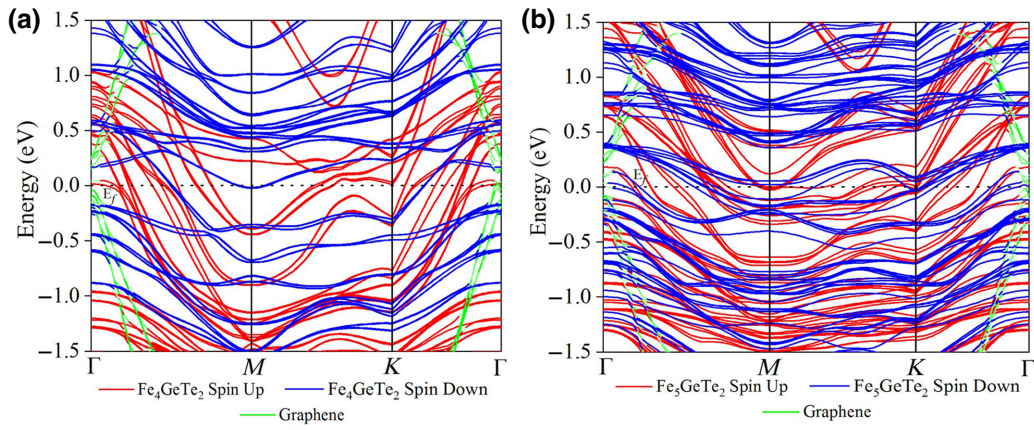


FIG. 6. Weight-projected band structure of Fe_4GeTe_2 /graphene/ Fe_4GeTe_2 MTJ (a) and Fe_5GeTe_2 /graphene/ Fe_5GeTe_2 MTJ (b). Fermi level is set to zero. Green lines represent the projected band weight on graphene.

in the Fe_3GeTe_2 /graphene/ Fe_3GeTe_2 MTJ. One feature is that the interaction brings about a small band gap at the Γ point of graphene, and the band gap in the Fe_4GeTe_2 /graphene/ Fe_4GeTe_2 MTJ is larger than that in Fe_5GeTe_2 /graphene/ Fe_5GeTe_2 . Previous research has reported a similar band gap opening at the Γ point in the GeS/graphene vdW heterostructure [48].

Projected local density of states (PLDOS) of the Fe_xGeTe_2 /graphene/ Fe_xGeTe_2 ($x = 4$ and 5) MTJs are

plotted in Figs. 7 and 8 to show the distribution of transmitted electrons in real space and the potential barrier height of each layer in the vdW MTJ. The potential profiles displayed by the green lines are approximately assumed to be the lowest energy level above the Fermi level, where $\log_{10}(\text{LDOS})$ is larger than $-1.2 \text{ eV}^{-1} \text{ \AA}^{-3}$. The main idea is that electrons with opposite spin to the magnetic layer encounter a higher potential barrier during transmission than the electrons with the same spin as the magnetic layer.

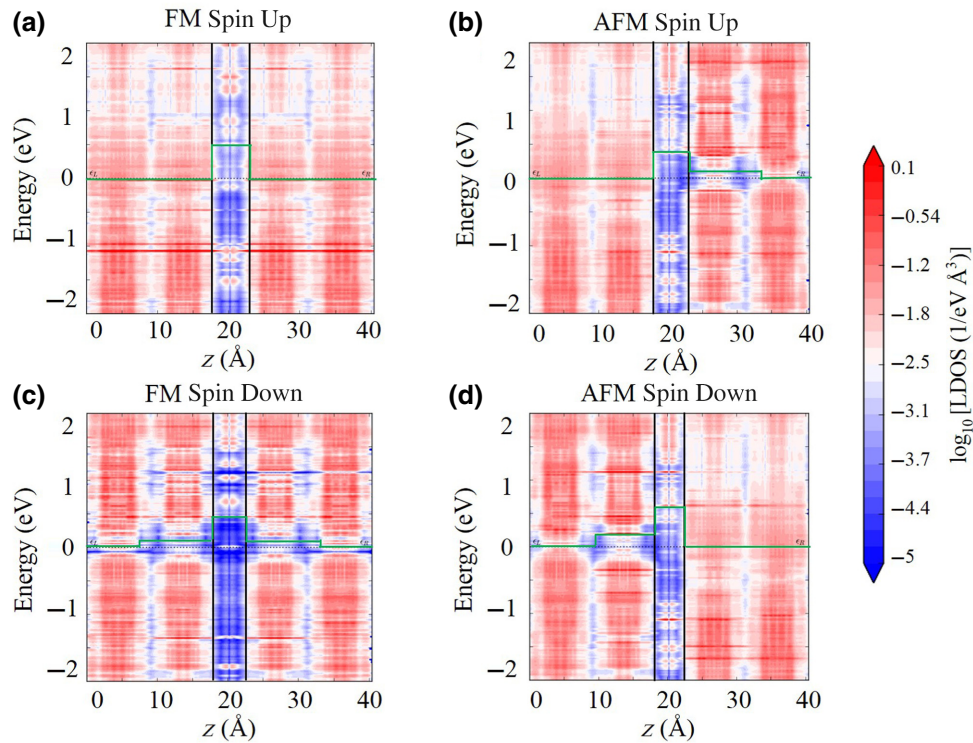


FIG. 7. Spin-resolved PLDOS of the Fe_4GeTe_2 /graphene/ Fe_4GeTe_2 MTJ in the FM ($\theta = 0^\circ$) and AFM ($\theta = 180^\circ$) states. Fermi level is set to zero energy. Black lines indicate the boundary lines of the electrode and the tunnel region, and green lines are the spin-dependent potential barrier profile.

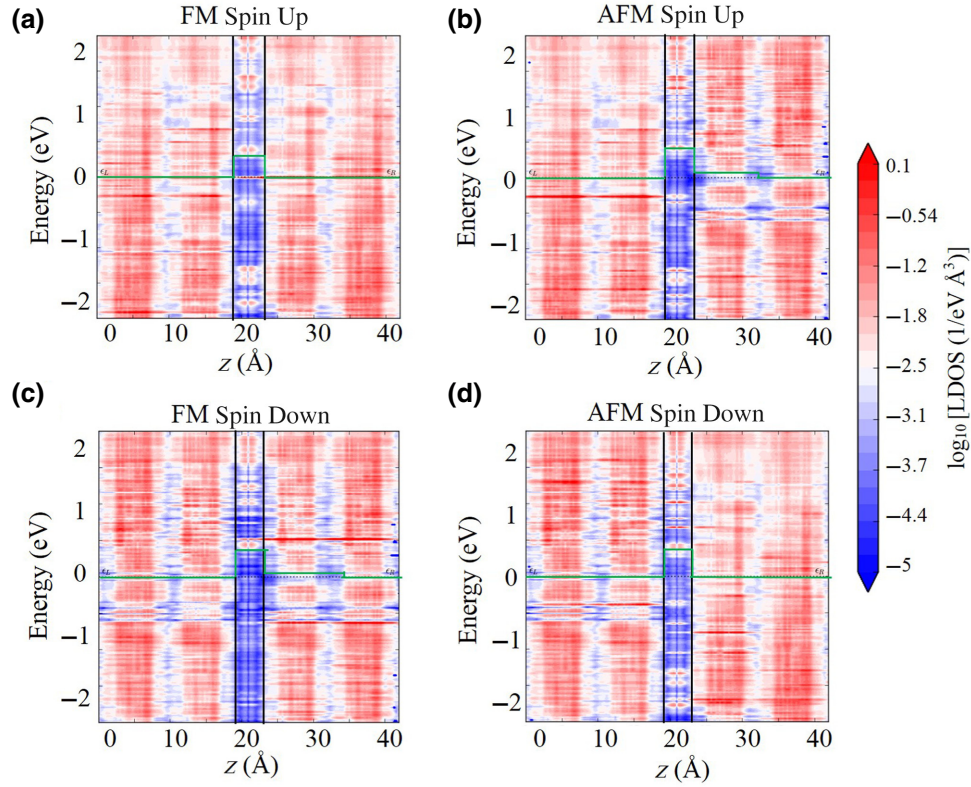


FIG. 8. Spin-resolved PLDOS of the $\text{Fe}_5\text{GeTe}_2/\text{graphene}/\text{Fe}_5\text{GeTe}_2$ MTJ in the FM ($\theta = 0^\circ$) and AFM ($\theta = 180^\circ$) states. Fermi level is set to zero energy. Black lines indicate the boundary lines of the electrode and the tunnel region, and green lines are the spin-dependent potential barrier profile.

This is also the meaning of the “spin-filtering effect.” The spin-filtering efficiency of the magnetic layer is generally positively correlated with its potential barrier height for opposite-spin electrons. In Figs. 7(c) and 8(c), we can see that the potential barrier height for opposite-spin electrons in the Fe_4GeTe_2 layer is higher than that in the Fe_5GeTe_2 layer. This also corresponds to the larger $P'_Z(0^\circ)$ of the $\text{Fe}_4\text{GeTe}_2/\text{graphene}/\text{Fe}_4\text{GeTe}_2$ MTJ. From Figs. 7(a) and 8(a), we can find that the tunnel barrier height of the graphene spacer (marked by the green line) in the $\text{Fe}_4\text{GeTe}_2/\text{graphene}/\text{Fe}_4\text{GeTe}_2$ MTJ is larger than that in the $\text{Fe}_5\text{GeTe}_2/\text{graphene}/\text{Fe}_5\text{GeTe}_2$ MTJ. This exactly corresponds to the larger band gap at the Γ point of the graphene spacer in the $\text{Fe}_4\text{GeTe}_2/\text{graphene}/\text{Fe}_4\text{GeTe}_2$ MTJ than that in the $\text{Fe}_5\text{GeTe}_2/\text{graphene}/\text{Fe}_5\text{GeTe}_2$ MTJ, as shown in Fig. 6.

The asymmetry of the PLDOS and $P'_Z(\theta)$ and nonzero $G_Z(180^\circ)$ in the $\text{Fe}_5\text{GeTe}_2/\text{graphene}/\text{Fe}_5\text{GeTe}_2$ MTJ are due to the asymmetric structure of the MTJ. We check that the optimized structure of the $\text{Fe}_4\text{GeTe}_2/\text{graphene}/\text{Fe}_4\text{GeTe}_2$ MTJ is strictly specularly symmetric with respect to the central graphene face. However, the optimized structure of the $\text{Fe}_5\text{GeTe}_2/\text{graphene}/\text{Fe}_5\text{GeTe}_2$ MTJ is not strictly specularly symmetric with respect to the central graphene face. The asymmetric

part is the relative position of the Ge atom and the Fe_1 atom (which is also the extra Fe atom compared with Fe_4GeTe_2), as shown in Fig. 1(d). In the left electrode, the Ge atoms are farther away from the graphene spacer than the Fe_1 atoms. Whereas in the right electrode, the Ge atoms are closer to the graphene spacer than the Fe_1 atoms. The reason for the asymmetric structure is that, as bulk Fe_5GeTe_2 has ABC -stacking order, there are actually three stable stacking orders for bilayer Fe_5GeTe_2 , that is, AB stacking, BC stacking, and CA stacking. In our initial structure, the left and right electrodes adopt the same stacking order. However, in our optimized structure of the $\text{Fe}_5\text{GeTe}_2/\text{graphene}/\text{Fe}_5\text{GeTe}_2$ MTJ, the left electrode and the right electrode adopt different stacking orders. This asymmetry leads to the asymmetric PLDOS and $P'_Z(\theta)$, which also indicates that the spin-filtering efficiency of differently stacked Fe_5GeTe_2 bilayers is different.

The θ -dependent TMR (referred to as R_{TMR}) is defined as [49]

$$R_{\text{TMR}}(\theta) = \frac{G_{\text{sum}}(0^\circ) - G_{\text{sum}}(\theta)}{G_{\text{sum}}(\theta)} \times 100\% \quad (20)$$

Note that the TMR we refer to in the collinear situation is equivalent to $\text{TMR}(180^\circ)$ in the noncollinear situation.

In practical experiments, the rotation of magnetization can be achieved by either applying an external magnetic field, like in the $\text{Fe}_3\text{GeTe}_2/h\text{-BN}/\text{Fe}_3\text{GeTe}_2$ case, which takes advantage of the difference in coercivity between the left and right electrodes [8], or utilizing the STT, as we discuss in Sec. III C.

Figure 2(f) exhibits the calculated $\text{TMR}(\theta)$, and we obtain a maximum TMR of 6800% when $\theta = 180^\circ$ in the $\text{Fe}_4\text{GeTe}_2/\text{graphene}/\text{Fe}_4\text{GeTe}_2$ MTJ, which is much larger than the calculated (1000%) and measured ($\sim 1000\%$) TMR of traditional MgO-based MTJs and the calculated ($\sim 200\%$, this work) and measured ($\sim 160\%$) TMR of the $\text{Fe}_3\text{GeTe}_2/h\text{-BN}/\text{Fe}_3\text{GeTe}_2$ MTJ [8,16,17]. The $\text{Fe}_5\text{GeTe}_2/\text{graphene}/\text{Fe}_5\text{GeTe}_2$ MTJs exhibit a maximal TMR of 1100% when $\theta = 180^\circ$. The different TMR of the $\text{Fe}_x\text{GeTe}_2/\text{graphene}/\text{Fe}_x\text{GeTe}_2$ ($x = 4$ and 5) MTJs can also be reflected by different k_{\parallel} -resolved transmission coefficients when $\theta = 0^\circ$ and 180° , as shown in Figs. 3 and 4. Note that the number of contributing transmission channels of the $\text{Fe}_5\text{GeTe}_2/\text{graphene}/\text{Fe}_5\text{GeTe}_2$ MTJ when $\theta = 180^\circ$ is smaller than that of the $\text{Fe}_4\text{GeTe}_2/\text{graphene}/\text{Fe}_4\text{GeTe}_2$ MTJ [$G_{\text{sum}}(180^\circ) 2.21 \times 10^{-4}(e^2/h)$ versus $5.64 \times 10^{-4}(e^2/h)$], the difference between the number of contributing channels is even bigger when $\theta = 0^\circ$ [$G_{\text{sum}}(0^\circ) 2.67 \times 10^{-3}(e^2/h)$ versus $3.91 \times 10^{-2}(e^2/h)$], resulting in the smaller TMR of the $\text{Fe}_5\text{GeTe}_2/\text{graphene}/\text{Fe}_5\text{GeTe}_2$ MTJ.

The factors that determine TMR are the combination of the factors that determine $G_{\sigma}(\theta)$ and $P_{\sigma}^t(\theta)$. From the perspective of the junction, although we cannot directly calculate η_s and η_e , we can infer them from computable $P_Z^t(0^\circ)$. Our calculated $P_Z^t(0^\circ)$ of the $\text{Fe}_x\text{GeTe}_2/\text{graphene}/\text{Fe}_x\text{GeTe}_2$ MTJs ($x = 3, 4$ and 5) is 22.8%, 97.8%, and 54%, respectively. Combined with the corresponding calculated maximal TMR (269%, 6800%, and 1100% in the same order), we can conclude that, for MTJs with the same spacer, TMR generally increases with increasing $P_Z^t(0^\circ)$. This result also agrees with Julliere's model qualitatively, which gives an approximate relationship between $\text{TMR}(180^\circ)$ and $P_Z^t(0^\circ)$ in the collinear situation as $\text{TMR}(180^\circ) = 2P_Z^t(0^\circ)^2/(1 - P_Z^t(0^\circ)^2)$ (see Sec. 6 of the Supplemental Material for a comparison of the calculated TMR and the TMR predicted by Julliere's model [27]) [50]. Note that Julliere's model is only presented here to roughly estimate the relationship between TMR

(180°) and $P_Z^t(0^\circ)$. Strictly speaking, Julliere's model is only applied to the amorphous barrier by assuming electrons with different momentum in the Brillouin zone have the same transmission probability. So, this model cannot precisely reflect the coherent transport in single-crystalline MTJs.

To further determine the role that the ML graphene spacer plays in the big TMR of the $\text{Fe}_4\text{GeTe}_2/\text{graphene}/\text{Fe}_4\text{GeTe}_2$ MTJ, we replace the ML graphene spacer with ML $h\text{-BN}$ and BL graphene (the structures are shown in Sec. 7 of the Supplemental Material [27]) and calculate the transport properties, as shown in Table I. Compared with the configuration with the ML graphene spacer, the MTJ with the ML $h\text{-BN}$ spacer exhibits larger $G_{\text{sum}}(0^\circ)$ and $G_{\text{sum}}(180^\circ)$, but about 1/6 TMR(180°). The main reason for the smaller TMR is that the spin-filtering effect of the ML graphene spacer combined with the electrodes is stronger than that of the ML $h\text{-BN}$ spacer combined with the electrodes, indicating a larger η_s of the ML graphene. For the MTJ with the BL graphene spacer, $G_{\text{sum}}(0^\circ)$, $G_{\text{sum}}(180^\circ)$, and TMR(180°) all decrease, mainly because of the sharply decreased contributing transmission channels when $\theta = 0^\circ$ [reflected by the much smaller $G_{\text{sum}}(0^\circ)$]. We also check the effect of the bias voltage on the collinear TMR in the $\text{Fe}_4\text{GeTe}_2/\text{graphene}/\text{Fe}_4\text{GeTe}_2$ MTJ (shown in Sec. 8 of the Supplemental Material [27]) and find that TMR generally decreases with increasing bias voltage; this behavior is consistent with the previously reported Fe/MgO/Fe MTJ [51].

C. Spin-dynamic behavior of

$\text{Fe}_x\text{GeTe}_2/\text{graphene}/\text{Fe}_x\text{GeTe}_2$ ($x = 4$ and 5) MTJs

Next we calculate the critical voltage, V_c , and current, I_c , for magnetization reversal of the electrode utilizing the STT-based method by using the macrospin approximation [42,47]:

$$V_c = \alpha E_{\text{MCA}}/T_z^{\text{max}}(\theta_m), \quad (21)$$

$$I_c = \frac{e^2}{h} t(\theta_m) V_c = G(\theta_m) V_c, \quad (22)$$

where α is the Gilbert damping factor, E_{MCA} is the magnetocrystalline anisotropy (MCA) energy, T_z^{max} is the maximal z component of the STT per voltage (referred to

TABLE I. Calculated total conductance at $E = E_F$ when $\theta = 0^\circ$ and 180° and the corresponding TMR(180°) for different MTJs. Gr stands for graphene.

MTJ structures	$G_{\text{sum}}(0^\circ) (e^2/h)$	$G_{\text{sum}}(180^\circ) (e^2/h)$	TMR(180°) (%)
$\text{Fe}_4\text{GeTe}_2/\text{Gr}/\text{Fe}_4\text{GeTe}_2$	3.91×10^{-2}	5.64×10^{-4}	6836
$\text{Fe}_5\text{GeTe}_2/\text{Gr}/\text{Fe}_5\text{GeTe}_2$	2.67×10^{-3}	2.21×10^{-4}	1110
$\text{Fe}_4\text{GeTe}_2/h\text{-BN}/\text{Fe}_4\text{GeTe}_2$	4.80×10^{-2}	4.35×10^{-3}	1004
$\text{Fe}_4\text{GeTe}_2/\text{BL_Gr}/\text{Fe}_4\text{GeTe}_2$	1.00×10^{-3}	1.47×10^{-4}	583

as T) in the right half (free layer) of the MTJ, and θ_m is the angle corresponding to T_z^{\max} . Figure 9(a) shows a schematic diagram of the current-induced STT in the MTJ.

α exactly corresponds to the damping term of the Landau-Lifshitz-Gilbert-Slonczwski equation describing

the spin-precession process [shown in Fig. 9(b)], which is written as [52]

$$\frac{d\mathbf{M}}{dt} = -|\gamma|\mathbf{M} \times \mathbf{H}_{\text{eff}} + \frac{\alpha}{M_s} \left(\mathbf{M} \times \frac{d\mathbf{M}}{dt} \right) + \mathbf{T}_{\text{STT}} \quad (23)$$

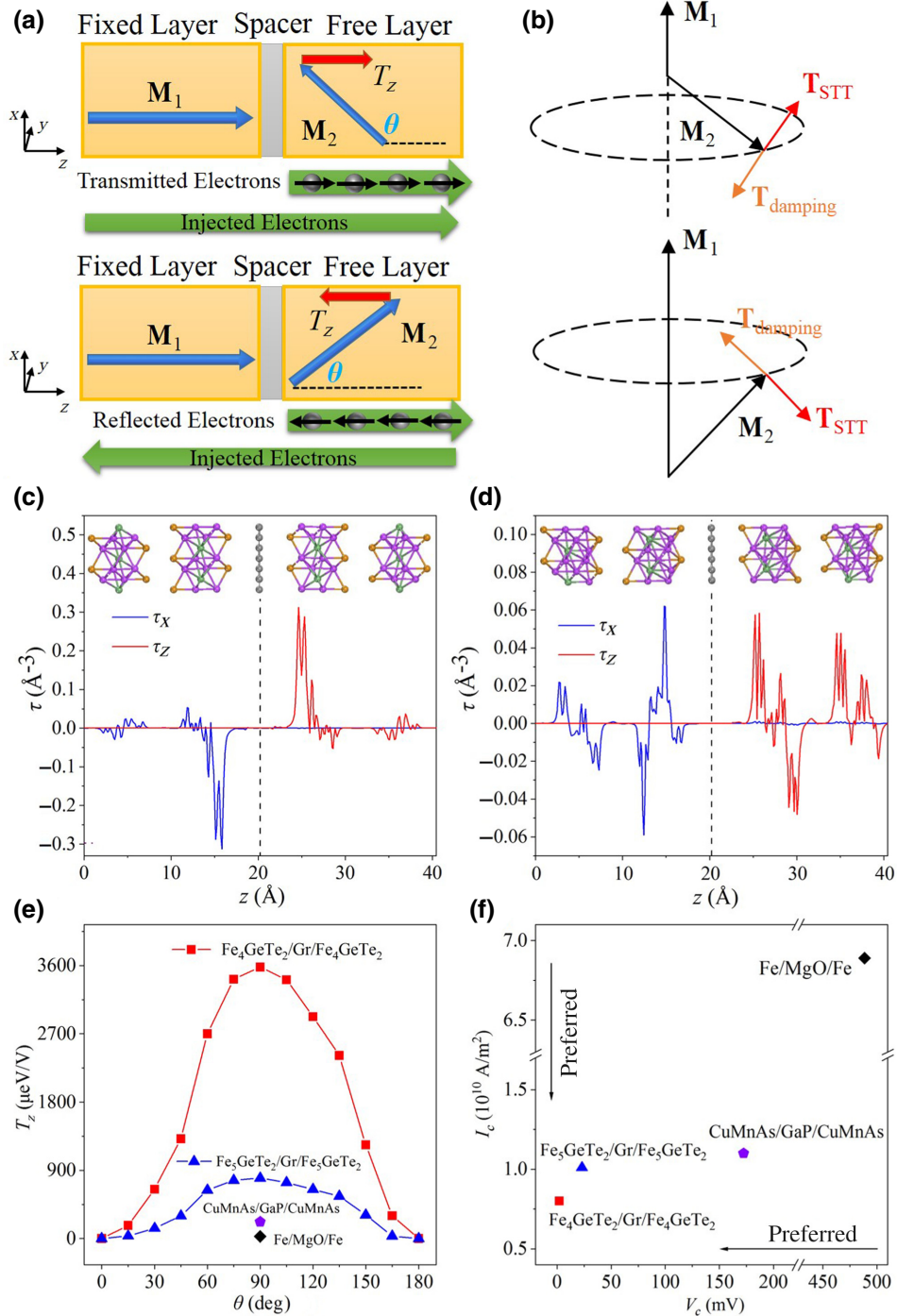


FIG. 9. Schematic diagram of the current-induced STT in the MTJ (a) and spin precession and reversal of the free layer (b). Distribution of the x and z components of spin-transfer torque τ in the $\text{Fe}_4\text{GeTe}_2/\text{graphene}/\text{Fe}_4\text{GeTe}_2$ MTJ (c) and $\text{Fe}_5\text{GeTe}_2/\text{graphene}/\text{Fe}_5\text{GeTe}_2$ MTJ (d). Dashed line represents the middle point of the device. (e) θ -dependent z component of the linear-response spin-transfer torque, T_z , of the $\text{Fe}_x\text{GeTe}_2/\text{graphene}/\text{Fe}_x\text{GeTe}_2$ ($x = 4$ and 5) MTJ. (f) Comparison of the predicted V_c and I_c of different MTJs.

where \mathbf{M} is the total magnetic moment, $|\gamma|$ is the Gilbert gyromagnetic ratio, \mathbf{H}_{eff} is the total effective magnetic field, M_s is the saturation magnetization, and \mathbf{T}_{STT} is the spin-transfer torque. A larger α means a larger \mathbf{T}_{STT} is needed to realize magnetization reversal, corresponding to a larger spin-polarized current. This explains why V_c and I_c are proportional to α in Eqs. (21) and (22), and an electrode material with a small α means lower power consumption. α of a material is mainly determined by the electronic structure at E_F and electron-phonon coupling. Figure S9 exhibits α of the BL Fe_xGeTe_2 ($x=4$ and 5) as a function of the lifetime broadening, Λ (see Sec. 9 of the Supplemental Material [27]). The minimum α values of BL Fe_4GeTe_2 and BL Fe_5GeTe_2 are 0.003 and 0.0036, respectively, which are approximately 1 order of magnitude smaller than the minimum α of commonly used bulk electrodes (0.021 for Fe and 0.027 for Co-Fe-B), as shown in Table II. The calculated α of BL Fe_5GeTe_2 is also very close to the experimental value (0.007) measured at 10 K [56], indicating the reliability of our calculations.

E_{MCA} measures the thermal stability of the magnetic states, which technologically corresponds to the non-volatility of the written information. Table II lists our calculated E_{MCA} and the normalized MCA constant K_1 (defined as E_{MCA}/A , where A is the cross-section area) of the $\text{Fe}_x\text{GeTe}_2/\text{graphene}/\text{Fe}_x\text{GeTe}_2$ ($x=4$ and 5) MTJs and makes a comparison with previously reported MTJs. Note that E_{MCA} here has two main contributions: MCA of the electrode itself and MCA of the electrode-spacer interface [57]. Previous experiments show that the W-capped Co-Fe-B/MgO/Co-Fe-B MTJ with 0.29 mJ/m^2 K_1 produces a thermal stability factor, Δ [defined as $(E_{\text{MCA}}/k_B T)$, if the magnetization is switched via uniform rotation], of 137, which is beyond the requirement ($\Delta > 67$) of 10-year data retention of STT MRAM [57,58]. As the vdW $\text{Fe}_x\text{GeTe}_2/\text{graphene}/\text{Fe}_x\text{GeTe}_2$ ($x=4$ and 5) MTJs generally possess several times larger K_1 (2.58 mJ/m^2 for $x=4$ and 5.76 mJ/m^2 for $x=5$) than that of the commonly used MgO-based MTJs, they will

produce much longer data storage times when applied in STT MRAM.

Only T_z is included in Eq. (21) for two reasons: one is that we focus on the magnetization in the x - z plane and neglect T_y ; the other is related to the detailed distribution of the x and z components of the STTK per unit volume (referred as τ) in the MTJs when $\theta = 90^\circ$, as shown in Figs. 9(c) and 9(d). \mathbf{T} can be obtained by integrating τ over the corresponding regions of the device. One noticeable feature is that τ_x and τ_z are approximately centrosymmetric about the midpoint of the device. This is because the left electrode and the right electrode with perpendicular magnetization directions are equivalent during the interaction process. When $\theta = 90^\circ$ in the left half of the device, τ_z is nearly 0, and in the right half of the device, τ_x is nearly 0. This indicates that the influence (STT) of one electrode on the other electrode is mainly distributed on the other half of the device and has the same direction as its own magnetization direction. As we fix the magnetization direction of the left electrode to the z axis, we use T_z to represent the effect of the fixed layer (left electrode) on the free layer (right electrode).

Another vital feature in Figs. 9(c) and 9(d) is that τ_x and τ_z reach a maximum at the inner layer and decrease sharply in the outer layer. This clearly indicates the decay of the staggered STTK with distance. This behavior is similar to that of the previously calculated STTK in the Cr/Cu/Cr spin valve [59] and the Cu-Mn-As/GaP/Cu-Mn-As MTJ [42] and is attributed to the interference of multiple contributing transmission channels with different k_{\parallel} at E_F . Note that the decay rate of the STTK in the Fe_5GeTe_2 -based MTJ is slower than that in the Fe_4GeTe_2 -based MTJ, so we assume that the decay rate of the STTK is related to the specific electrode material.

Figure 9(e) exhibits the effect of θ on T_z . The variation tendency is basically in the form of $\sin(\theta)$, which agrees with the theoretical derivation [47]. When $\theta = 90^\circ$, T_z in both MTJs reaches a maximum (i.e., $\theta_m = 90^\circ$). The values and comparison with typical

TABLE II. Gilbert damping factor, α ; maximal magnetocrystalline anisotropic energy, E_{MCA} ; cross-section area, A ; MCA constant, K_1 ; z component of the STT per voltage in the right half of the device, T_z ; critical voltage for magnetization reversal, V_c ; total transmission function at the Fermi level, t_F ; and the critical current density for magnetization reversal, I_c , of the $\text{Fe}_x\text{GeTe}_2/\text{graphene}/\text{Fe}_x\text{GeTe}_2$ ($x=4$ and 5) MTJ when $\theta = 90^\circ$. Corresponding experimental and theoretical figures of merit of the Cu-Mn-As/GaP/Cu-Mn-As, Fe/MgO/Fe and Co-Fe-B/MgO/Co-Fe-B MTJs are provided for comparison [42,44,53–55].

	α	E_{MCA} (meV)	A (\AA^2)	K_1 (mJ/m^2)	T_z ($\mu\text{eV/V}$)	V_c (mV)	t_F	I_c (10^{10} A/m^2)	Ref.
$\text{Fe}_4\text{GeTe}_2/\text{Gr}/\text{Fe}_4\text{GeTe}_2$	0.003	2.28	14.15	2.58	3580	1.9	1.52×10^{-2}	0.80	This work
$\text{Fe}_5\text{GeTe}_2/\text{Gr}/\text{Fe}_5\text{GeTe}_2$	0.0036	5.10	14.15	5.76	798	22.9	1.61×10^{-3}	1.01	This work
Cu-Mn-As/GaP/Cu-Mn-As	0.1	0.381	14.59	0.42	221	172.4	2.40×10^{-4}	1.10	[42]
Fe/MgO/Fe	0.021 ^a	0.685	8.21	1.33	29.4	488.6	3.0×10^{-4}	6.89	[44,53]
Co-Fe-B/MgO/Co-Fe-B	0.027 ^a	8.47×10^3	5.04×10^5	0.29 ^a	—	—	—	3.9, ^a 5.0	[54,55]

^aExperimental figures of merit of the Cu-Mn-As/GaP/Cu-Mn-As, Fe/MgO/Fe and Co-Fe-B/MgO/Co-Fe-B MTJs.

bulk-based MTJs are provided in Table II. The much larger current-induced STT in the Fe_xGeTe_2 -based MTJs is attributed to two reasons. One is that $P_z^l(0^\circ)$ of the vdW $\text{Fe}_x\text{GeTe}_2/\text{graphene}/\text{Fe}_x\text{GeTe}_2$ ($x = 4$ and 5) MTJs is generally larger than that of the MgO-based MTJs. Currents with higher spin polarizability possess higher STT transmission efficiency. The other point is that, due to the weak interlayer interaction, it is easier to flip the magnetization direction of one specific layer in 2D vdW magnets than in bulk magnets with strong interlayer coupling. As the current-induced STT corresponds to the change rate of the spin angular momentum with time, it is larger in the 2D vdW magnets.

The calculated V_c and I_c values based on Eqs. (21) and (22) are compared with those of the typical bulk-based MTJs in Table II and Fig. 9(f). The theoretically predicted I_c (5.0×10^{10} A/m²) of the Co-Fe-B/MgO/Co-Fe-B MTJ utilizing the macrospin approximation is close to the experimental one (3.9×10^{10} A/m²), indicating the reliability of Eqs. (21) and (22) [54,55]. The calculated I_c of the Fe_xGeTe_2 -based MTJ (0.8×10^{10} A/m² for $x = 4$ and 1.01×10^{10} A/m² for $x = 5$) is only about 1/8–1/7 of the calculated one (6.89×10^{10} A/m²) of the Fe/MgO/Fe MTJ and 1/5–1/4 of the calculated and observed one of the Co-Fe-B/MgO/Co-Fe-B MTJ, mainly due to the smaller α and much larger T_z . Such a low I_c will significantly lower the power consumption, reduce the thermal effect, and increase the service life of STT MRAM. We notice that, although the calculated V_c (1.9 mV for $x = 4$ and 22.9 mV for $x = 5$) of the Fe_xGeTe_2 -based MTJ is approximately 1/257–1/21 of the calculated V_c (488.6 mV) of the Fe/MgO/Fe MTJs, the much larger t_F of the Fe_xGeTe_2 -based MTJ (1.52×10^{-2} for $x = 4$ and 1.61×10^{-3} for $x = 5$ versus 3.0×10^{-4} for the Fe/MgO/Fe MTJ) narrows the gap of I_c . Therefore, decreasing t_F (defined as the transmission function at $E = E_F$) without significantly affecting T_z is a possible way to reduce I_c further.

IV. CONCLUSION

We reveal a monotonic increasing tendency of the TMR with increasing θ in Fe_xGeTe_2 -based ($x = 4$ and 5) MTJs from *ab initio* quantum transport simulations. Compared with the commonly used MgO-based MTJs, the maximum TMR increases by 6 times (7000%) for $x = 4$ due to the much larger spin polarizability. The calculated maximal STT per voltage is 2 (1) orders of magnitude larger for $x = 4$ (5), leading to a much reduced critical voltage and current for magnetization reversal. Therefore, the Fe_xGeTe_2 -based ($x = 4$ and 5) MTJs perform better and are potential candidates for next-generation room-temperature spintronic devices.

Data that support the findings of this study are available within the article and its Supplemental Material [27].

ACKNOWLEDGMENT

This work is supported by the National Natural Science Foundation of China (Grant No. 12241401, No. 11975035, No. 91964101, No. 51731001, and No. 12274002), the Fundamental Research Funds for the Central Universities, the High-Performance Computing Platform of Peking University, and the Ministry of Science and Technology of China (2022YFA1200072). B.C.W., F.S.B., J.L., H.L.D., and J.B.Y. conceived the work and organized the manuscript. B.C.W. and S.B.F. did the calculations and collated all the data. J.Y., S.Q.L., Y.X.P., Q.H.L., Z.C.L., W.Y.Y., Z.C.L., and C.S.W. helped analyze the data. B.C.W. and S.B.F. wrote the original manuscript. All authors contributed to the discussion of the results and manuscript revision.

The authors declare no conflict of interest.

- [1] M. F. Khan, H. Kim, G. Nazir, S. Jung, and J. Eom, Layer dependent magnetoresistance of vertical MoS₂ magnetic tunnel junctions, *Nanoscale* **10**, 16703 (2018).
- [2] H. Dery, P. Dalal, L. Cywinski, and L. J. Sham, Spin-based logic in semiconductors for reconfigurable large-scale circuits, *Nature* **447**, 573 (2007).
- [3] B. Behin-Aein, D. Datta, S. Salahuddin, and S. Datta, Proposal for an all-spin logic device with built-in memory, *Nat. Nanotechnol.* **5**, 266 (2010).
- [4] C. Gong and X. Zhang, Two-dimensional magnetic crystals and emergent heterostructure devices, *Science* **363**, 706 (2019).
- [5] M. Gibertini, M. Koperski, A. F. Morpurgo, and K. S. Novoselov, Magnetic 2D materials and heterostructures, *Nat. Nanotechnol.* **14**, 408 (2019).
- [6] Z. Guo, J. Yin, Y. Bai, D. Zhu, K. Shi, G. Wang, K. Cao, and W. Zhao, Spintronics for energy-efficient computing: An overview and outlook, *Proc. IEEE* **109**, 1398 (2021).
- [7] L. Zhang, J. Zhou, H. Li, L. Shen, and Y. P. Feng, Recent progress and challenges in magnetic tunnel junctions with 2D materials for spintronic applications, *Appl. Phys. Rev.* **8**, 021308 (2021).
- [8] Z. Wang, D. Sapkota, T. Taniguchi, K. Watanabe, D. Mandrus, and A. F. Morpurgo, Tunneling spin valves based on Fe₃GeTe₂/hBN/Fe₃GeTe₂ van der Waals heterostructures, *Nano Lett.* **18**, 4303 (2018).
- [9] Y. Wang, S. Liu, Q. Li, R. Quhe, C. Yang, Y. Guo, X. Zhang, Y. Pan, J. Li, H. Zhang, *et al.*, Schottky barrier heights in two-dimensional field-effect transistors: From theory to experiment, *Rep. Prog. Phys.* **84**, 056501 (2021).
- [10] R. Quhe, *et al.*, Sub-10 nm two-dimensional transistors: Theory and experiment, *Phys. Rep.* **938**, 1 (2021).
- [11] Y. Peng, X. Cheng, P. Gu, F. Wang, J. Yang, M. Xue, W. Yang, C. Wang, S. Liu, K. Watanabe, *et al.*, A quaternary van der Waals ferromagnetic semiconductor AgVP₂Se₆, *Adv. Funct. Mater.* **30**, 1910036 (2020).
- [12] Y. Peng, S. Ding, M. Cheng, Q. Hu, J. Yang, F. Wang, M. Xue, Z. Liu, Z. Lin, M. Avdeev, *et al.*, Magnetic structure and metamagnetic transitions in the van der Waals antiferromagnet CrPS₄, *Adv. Mater.* **32**, 2001200 (2020).

- [13] S. Ding, Z. Liang, J. Yang, C. Yun, P. Zhang, Z. Li, M. Xue, Z. Liu, G. Tian, F. Liu, *et al.*, Ferromagnetism in two-dimensional Fe_3GeTe_2 ; Tunability by hydrostatic pressure, *Phys. Rev. B* **103**, 094429 (2021).
- [14] B. Wu, J. Yang, R. Quhe, S. Liu, C. Yang, Q. Li, J. Ma, Y. Peng, S. Fang, J. Shi, *et al.*, Scaling Behavior of Magnetoresistance with the Layer Number in CrI_3 Magnetic Tunnel Junctions, *Phys. Rev. Appl.* **17**, 034030 (2022).
- [15] H. H. Kim, B. Yang, T. Patel, F. Sfigakis, C. Li, S. Tian, H. Lei, and A. W. Tsien, One million percent tunnel magnetoresistance in a magnetic van der Waals heterostructure, *Nano Lett.* **18**, 4885 (2018).
- [16] S. Yuasa and D. D. Djayaprawira, Giant tunnel magnetoresistance in magnetic tunnel junctions with a crystalline $\text{MgO}(001)$ barrier, *J. Phys. D: Appl. Phys.* **40**, R337 (2007).
- [17] W. H. Butler, X. G. Zhang, T. C. Schulthess, and J. M. MacLaren, Spin-dependent tunneling conductance of $\text{Fe}|\text{MgO}|\text{Fe}$ sandwiches, *Phys. Rev. B* **63**, 054416 (2001).
- [18] C. Gong, L. Li, Z. Li, H. Ji, A. Stern, Y. Xia, T. Cao, W. Bao, C. Wang, Y. Wang, *et al.*, Discovery of intrinsic ferromagnetism in two-dimensional van der Waals crystals, *Nature* **546**, 265 (2017).
- [19] B. Huang, G. Clark, E. Navarro-Moratalla, D. R. Klein, R. Cheng, K. L. Seyler, D. Zhong, E. Schmidgall, M. A. McGuire, D. H. Cobden, *et al.*, Layer-dependent ferromagnetism in a van der Waals crystal down to the monolayer limit, *Nature* **546**, 270 (2017).
- [20] Y. Deng, Y. Yu, Y. Song, J. Zhang, N. Z. Wang, Z. Sun, Y. Yi, Y. Z. Wu, S. Wu, J. Zhu, *et al.*, Gate-tunable room-temperature ferromagnetism in two-dimensional Fe_3GeTe_2 , *Nature* **563**, 94 (2018).
- [21] Z. Fei, B. Huang, P. Malinowski, W. Wang, T. Song, J. Sanchez, W. Yao, D. Xiao, X. Zhu, A. F. May, *et al.*, Two-dimensional itinerant ferromagnetism in atomically thin Fe_3GeTe_2 , *Nat. Mater.* **17**, 778 (2018).
- [22] A. F. May, D. Ovchinnikov, Q. Zheng, R. Hermann, S. Calder, B. Huang, Z. Fei, Y. Liu, X. Xu, and M. A. McGuire, Ferromagnetism near room temperature in the cleavable van der Waals crystal Fe_5GeTe_2 , *ACS Nano* **13**, 4436 (2019).
- [23] J. Stahl, E. Shlaen, and D. Johrendt, The van der Waals ferromagnets $\text{Fe}_{5-\delta}\text{GeTe}_2$ and $\text{Fe}_{5-\delta-x}\text{Ni}_x\text{GeTe}_2$ – crystal structure, stacking faults, and magnetic properties, *Z. Anorg. Allg. Chem.* **644**, 1923 (2018).
- [24] J. Seo, *et al.*, Nearly room temperature ferromagnetism in a magnetic metal-rich van der Waals metal, *Sci. Adv.* **6**, eaay8912 (2020).
- [25] T. C. Song, X. H. Cai, M. W. Y. Tu, X. O. Zhang, B. V. Huang, N. P. Wilson, K. L. Seyler, L. Zhu, T. Taniguchi, K. Watanabe, *et al.*, Giant tunneling magnetoresistance in spin-filter van der Waals heterostructures, *Science* **360**, 1214 (2018).
- [26] D. R. Klein, D. MacNeill, J. L. Lado, D. Soriano, E. Navarro-Moratalla, K. Watanabe, T. Taniguchi, S. Manni, P. Canfield, J. Fernández-Rossier, and P. Jarillo-Herrero, Probing magnetism in 2D van der Waals crystalline insulators via electron tunneling, *Science* **360**, 1218 (2018).
- [27] See the Supplemental Information at <http://link.aps.org/supplemental/10.1103/PhysRevApplied.19.024037> for geometric structures of Fe_xGeTe_2 ($x=3, 4$, and 5), band structures and DOS of BL Fe_xGeTe_2 ($x=4$ and 5) with SOC correction, band structures and DOS of ABC -stacking and AB -stacking bulk Fe_xGeTe_2 ($x=4$ and 5), test of k -point convergence, spin-resolved transmission eigenstate, comparison of the calculated TMR and the TMR predicted by Julliere's model, geometric structures of $\text{Fe}_4\text{GeTe}_2/\text{BLGr}/\text{Fe}_4\text{GeTe}_2$ MTJ and $\text{Fe}_4\text{GeTe}_2/h\text{-BN}/\text{Fe}_4\text{GeTe}_2$ MTJ, effect of the bias voltage on TMR, Gilbert damping factor of BL Fe_xGeTe_2 ($x=4$ and 5), interface between Fe_xGeTe_2 ($x=4$ and 5) and graphene, transport properties of the calculated $\text{Fe}_3\text{GeTe}_2/h\text{-BN}/\text{Fe}_3\text{GeTe}_2$ MTJ, and symmetry analysis of the BL Fe_xGeTe_2 ($x=4$ and 5) electrodes.
- [28] J. P. Perdew, K. Burke, and M. Ernzerhof, Generalized Gradient Approximation Made Simple, *Phys. Rev. Lett.* **77**, 3865 (1996).
- [29] P. E. Blochl, Projector augmented-wave method, *Phys. Rev. B* **50**, 17953 (1994).
- [30] G. Kresse and D. Joubert, From ultrasoft pseudopotentials to the projector augmented-wave method, *Phys. Rev. B* **59**, 1758 (1999).
- [31] G. Kresse and J. Hafner, *Ab-initio* molecular-dynamics for open-shell transition-metals, *Phys. Rev. B* **48**, 13115 (1993).
- [32] M. Joe, U. Yang, and C. Lee, First-principles study of ferromagnetic metal Fe_5GeTe_2 , *Nano Mater. Sci.* **1**, 299 (2019).
- [33] M. Brandbyge, J. L. Mozos, P. Ordejon, J. Taylor, and K. Stokbro, Density-functional method for nonequilibrium electron transport, *Phys. Rev. B* **65**, 165401 (2002).
- [34] J. M. Soler, E. Artacho, J. D. Gale, A. Garcia, J. Junquera, P. Ordejon, and D. Sanchez-Portal, The SIESTA method for *ab initio* order- N materials simulation, *J. Phys. Condens. Matter* **14**, 2745 (2002).
- [35] Y. Wang, J. Zheng, Z. Ni, R. Fei, Q. Liu, R. Quhe, C. Xu, J. Zhou, Z. Gao, and J. Lu, Half-metallic silicene and germanene nanoribbons: Towards high-performance spintronics device, *NANO* **07**, 1250037 (2012).
- [36] B. Wu, R. Quhe, J. Yang, S. Liu, J. Shi, J. Lu, and H. Du, High-performance spin filters and spin field effect transistors based on bilayer VSe_2 , *Adv. Theory Simul.* **4**, 2000238 (2020).
- [37] J. Yang, S. Fang, Y. Peng, S. Liu, B. Wu, R. Quhe, S. Ding, C. Yang, J. Ma, B. Shi, *et al.*, Layer-Dependent Giant Magnetoresistance in Two-Dimensional CrPS_4 Magnetic Tunnel Junctions, *Phys. Rev. Appl.* **16**, 024011 (2021).
- [38] K. Gilmore, Y. U. Idzerda, and M. D. Stiles, Identification of the Dominant Precession-Damping Mechanism in Fe, Co, and Ni by First-Principles Calculations, *Phys. Rev. Lett.* **99**, 027204 (2007).
- [39] D. Thonig, Y. Kvashnin, O. Eriksson, and M. Pereiro, Nonlocal Gilbert damping tensor within the torque-torque correlation model, *Phys. Rev. Mater.* **2**, 013801 (2018).
- [40] R. K. Ghosh, A. Jose, and G. Kumari, Intrinsic spin-dynamical properties of two-dimensional half-metallic FeX_2 ($X = \text{Cl, Br, I}$) ferromagnets: Insight from density functional theory calculations, *Phys. Rev. B* **103**, 054409 (2021).
- [41] M. Stamenova, P. Stamenov, F. Mahfouzi, Q. Sun, N. Kioussis, and S. Sanvito, Spin-transfer torque in

- Mn₃Ga-based ferrimagnetic tunnel junctions from first principles, *Phys. Rev. B* **103**, 094403 (2021).
- [42] M. Stamenova, R. Mohebbi, J. Seyed-Yazdi, I. Rungger, and S. Sanvito, First-principles spin-transfer torque in CuMnAs/GaP/CuMnAs junctions, *Phys. Rev. B* **95**, 060403 (2017).
- [43] X. Li, J. T. Lu, J. Zhang, L. You, Y. Su, and E. Y. Tsymbal, Spin-dependent transport in van der Waals magnetic tunnel junctions with Fe₃GeTe₂ electrodes, *Nano Lett.* **19**, 5133 (2019).
- [44] C. Heiliger and M. D. Stiles, *Ab Initio* Studies of the Spin-Transfer Torque in Magnetic Tunnel Junctions, *Phys. Rev. Lett.* **100**, 186805 (2008).
- [45] J. C. Sankey, Y.-T. Cui, J. Z. Sun, J. C. Slonczewski, R. A. Buhrman, and D. C. Ralph, Measurement of the spin-transfer torque vector in magnetic tunnel junctions, *Nat. Phys.* **4**, 67 (2007).
- [46] Y. Su, X. Li, M. Zhu, J. Zhang, L. You, and E. Y. Tsymbal, van der Waals multiferroic tunnel junctions, *Nano Lett.* **21**, 175 (2021).
- [47] D. C. Ralph and M. D. Stiles, Spin-transfer torques, *J. Magn. Magn. Mater.* **320**, 1190 (2008).
- [48] H. Chen, J. Zhao, J. Huang, and Y. Liang, Computational understanding of the structural and electronic properties of the GeS-graphene contact, *Phys. Chem. Chem. Phys.* **21**, 7447 (2019).
- [49] X. Jia, K. Xia, Y. Ke, and H. Guo, Nonlinear bias dependence of spin-transfer torque from atomic first principles, *Phys. Rev. B* **84**, 014401 (2011).
- [50] M. Julliere, Tunneling between ferromagnetic films, *Phys. Lett. A* **54**, 225 (1975).
- [51] D. Waldron, V. Timoshevskii, Y. Hu, K. Xia, and H. Guo, First Principles Modeling of Tunnel Magnetoresistance of Fe/MgO/Fe Trilayers, *Phys. Rev. Lett.* **97**, 226802 (2006).
- [52] J. C. Slonczewski, Current-driven excitation of magnetic multilayers, *J. Magn. Magn. Mater.* **159**, L1 (1996).
- [53] L. Chen, S. Mankovsky, S. Wimmer, M. A. W. Schoen, H. S. Körner, M. Kronseder, D. Schuh, D. Bougeard, H. Ebert, D. Weiss, and C. H. Back, Emergence of anisotropic Gilbert damping in ultrathin Fe layers on GaAs(001), *Nat. Phys.* **14**, 490 (2018).
- [54] S. Ikeda, K. Miura, H. Yamamoto, K. Mizunuma, H. D. Gan, M. Endo, S. Kanai, J. Hayakawa, F. Matsukura, and H. Ohno, A perpendicular-anisotropy CoFeB-MgO magnetic tunnel junction, *Nat. Mater.* **9**, 721 (2010).
- [55] C.-T. Yen, W.-C. Chen, D.-Y. Wang, Y.-J. Lee, C.-T. Shen, S.-Y. Yang, C.-H. Tsai, C.-C. Hung, K.-H. Shen, M.-J. Tsai, and M.-J. Kao, Reduction in critical current density for spin torque transfer switching with composite free layer, *Appl. Phys. Lett.* **93**, 092504 (2008).
- [56] L. Alahmed, B. Nepal, J. Macy, W. Zheng, B. Casas, A. Sapkota, N. Jones, A. R. Mazza, M. Brahlek, W. Jin, *et al.*, Magnetism and spin dynamics in room-temperature van der Waals magnet Fe₅GeTe₂, *2D Mater.* **8**, 045030 (2021).
- [57] A. V. Khvalkovskiy, D. Apalkov, S. Watts, R. Chepulsikii, R. S. Beach, A. Ong, X. Tang, A. Driskill-Smith, W. H. Butler, P. B. Visscher, *et al.*, Erratum: Basic principles of STT-MRAM cell operation in memory arrays, *J. Phys. D: Appl. Phys.* **46**, 139601 (2013).
- [58] Y. Liu, T. Yu, Z. Zhu, H. Zhong, K. M. Khamis, and K. Zhu, High thermal stability in W/MgO/CoFeB/W/CoFeB/W stacks via ultrathin W insertion with perpendicular magnetic anisotropy, *J. Magn. Magn. Mater.* **410**, 123 (2016).
- [59] P. M. Haney, D. Waldron, R. A. Duine, A. S. Núñez, H. Guo, and A. H. MacDonald, *Ab initio* giant magnetoresistance and current-induced torques in Cr/Au/Cr multilayers, *Phys. Rev. B* **75**, 174428 (2007).